

Semiconductor quantum-limited amplifier

D. Phan,¹ P. Falthansl-Scheinecker,¹ U. Mishra,¹ W.M. Strickland,² D. Langone,² J. Shabani,² and A.P. Higginbotham¹

¹*IST Austria, Am Campus 1, 3400 Klosterneuburg, Austria*

²*Center for Quantum Information Physics, Department of Physics, New York University, New York, NY, 10003, USA*

(Dated: October 27, 2022)

We have built a parametric amplifier with a Josephson field effect transistor (JoFET) as the active element. The device's resonant frequency is field-effect tunable over a range of 2 GHz. The JoFET amplifier has 20 dB of gain, 4 MHz of instantaneous bandwidth, and a 1 dB compression point of several photons when operated at a fixed resonance frequency. The amplifier's noise performance approaches the limits imposed by quantum mechanics. Magnetic-field compatibility and opportunities for sensing are discussed.

I. INTRODUCTION

Quantum-limited amplifiers are, for many experimental platforms, the first link in the quantum signal processing chain, allowing minute signals to be measured by noisy, classical electronics [1–3]. Whereas later parts of the chain are dominated by semiconductor-based devices, the quantum-limited step can currently only be performed using metallic superconductors [4–12]. Aluminum-oxide based tunnel junctions have proven to be more reliable and stable than any other platform, thanks to the formation of pristine Al-AIO_x interfaces through the natural oxidization of Al.

A comparable natural, coherent, and scalable interface between a superconductor and a semiconductor was only recently introduced in the form of aluminum-InAs (Al-InAs) two-dimensional electron gas heterostructures [13–15]. Josephson junctions fabricated on these materials yield a voltage-controllable supercurrent with highly transparent contacts between Al and InAs quantum wells [16–18]. Al-InAs has recently been instrumental in exploring topological superconductivity [19–22], mesoscopic superconductivity [23] and voltage-tunable superconducting qubits [24].

More broadly, the inherent scalability of semiconductors has motivated a great deal of research on quantum applications, including the scalable generation of quantum-control signals [25–28], the processing of quantum information [24, 29] at fault-tolerant thresholds [30–34].

Here, we introduce Al-InAs as the basis for quantum-limited signal processing devices. We demonstrate a quantum-limited amplifier using an Al-InAs Josephson field-effect transistor (JoFET) as the active element. Our device has a resonant frequency tunable over 2 GHz via the field effect. In optimal operating ranges, the JoFET amplifier has 20 dB of gain with a 4 MHz instantaneous bandwidth. The gain is sufficient for integration into a measurement chain with conventional semiconductor amplifiers. Accordingly, we demonstrate a total added noise that approaches the fundamental limits placed by quantum mechanics. In contrast to metallic superconducting

amplifiers, our approach is compatible with parallel magnetic fields and can be used as a detector for voltages from a high-impedance source. The JoFET amplifier completes the suite of semiconductor-based options for quantum control, information processing, and readout.

II. DEVICE DESIGN

The JoFET amplifier is implemented as a half-wave coplanar waveguide (CPW) resonator with a gated superconductor-semiconductor hybrid Josephson field-effect-transistor positioned at the voltage node [Fig.1(a)]. Ground planes of the device are formed from 50 nm thin film Nb with 1 μm -squared flux-pinning holes near the edges to improve magnetic-field resilience [35, 36]. The entire center pin of the resonator is made of Al-InAs heterostructure, defined by chemical etch. The JoFET is defined by selective removal of the Al, followed by atomic layer deposition of alumina, and finally an electrostatic gate is defined with electron beam lithography and Au evaporation. Eventually, large Au chip-to-chip bond pads are also co-deposited in the final step to improve wire-bonding yield. The characteristic impedance of the CPW is designed to be near 50 Ω with 25 μm wide center conductor width and a 16 μm gap to the ground plane. The device is capacitively coupled to an open 50 Ω transmission line, which forms the only measurement port.

We targeted a geometric resonant frequency of 6 GHz for compatibility with the standard 4 – 8 GHz band used in circuit quantum electrodynamics experiments. In designing the circuit, it is important to account for the kinetic inductance of the Al-InAs heterostructure [37], which typically causes a 20% reduction in the circuit resonant frequency. The device is therefore designed with a geometric resonant frequency of 7.2 GHz, corresponding to a CPW resonator length of 8 mm.

The external coupling κ_{ex} and the critical current I_C determine the operating bandwidth and dynamic range of the amplifier [38]. While κ_{ex} can be estimated from the circuit geometry, I_C is more subtle because it depends on material details. Based on independent transport tests,

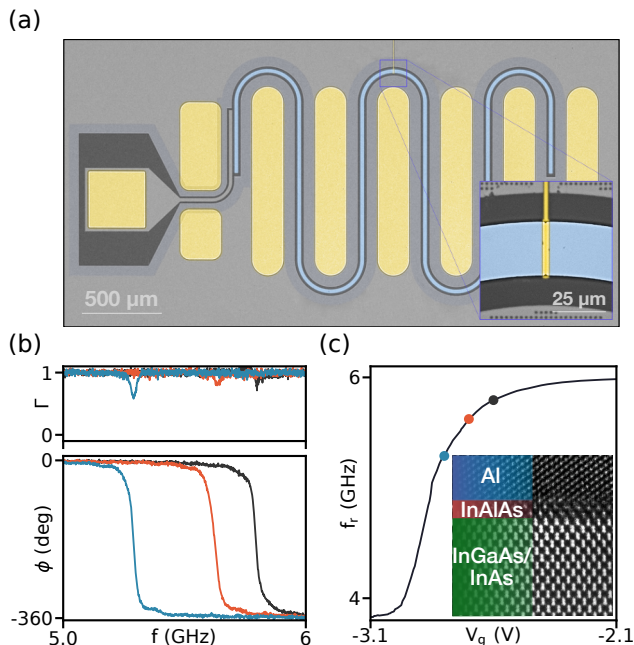


Figure 1. Device and frequency modulation via the field effect. (a) False-colored image of the device (InP substrate dark gray, Nb light gray, aluminum light blue, Au yellow). A feed line (left) capacitively couples to the resonator, which is formed from an Al-InAs semiconductor heterostructure. Inset: Image of JoFET and electrostatic gate. (b) Reflected signal magnitude Γ (top) and phase ϕ (bottom) versus signal frequency f at three different gate voltages V_g : -2.6 V (black), -2.7 V (orange), -2.8 V (blue), showing shift of resonance frequency with decreasing gate voltage. (c) Resonant frequency f_r as a function of gate voltage V_g . Three dots with corresponding colors represent the three gate voltages in (d). Inset: Cross-sectional transmission electron micrograph at the interface of Al thin film and InAs quantum well. The contrast and brightness have been enhanced for clarity.

we found that a JoFET with a width of $25 \mu\text{m}$ have an expected critical current of $10 \mu\text{A}$ at positive gate voltages. Combined with our designed external coupling of $2\pi \times 14$ MHz this is expected to give a Kerr nonlinearity of approximately -3 kHz and a 1 dB compression point of a few photons with 20 dB of gain, which is suitable for parametric amplification [38].

III. GATE TUNABILITY

The microwave reflection coefficient $R = \Gamma e^{i\phi}$ of a small incident signal is measured from the sample in a dilution refrigerator with a standard measurement chain, including a cryogenic commercial high-electron mobility transistor amplifier (HEMT). The measured reflection coefficient displays a small dip in magnitude and a 360° winding of phase, signaling that the resonator is strongly coupled to the measurement port and that dissipation is weak [Fig. 1(b)]. Indeed, fitting the reflection coefficient

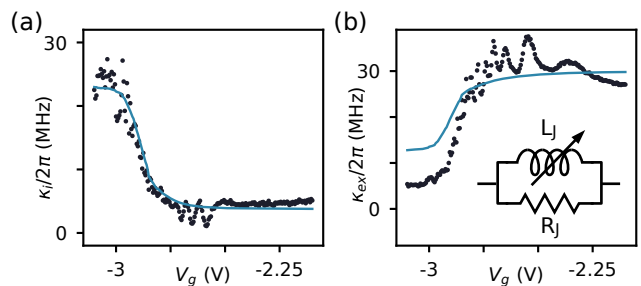


Figure 2. Circuit model. External coupling κ_{ex} (a) and internal loss rate κ_i (b) versus gate voltage V_g . Experimental data indicated by black points, and results of parallel RL model indicated by blue line. Inset: Proposed JoFET linear-equivalent circuit, consisting of tunable inductance L_J and fixed shunt resistance R_J in parallel.

to a one-port model gives an external coupling efficiency $\kappa_{\text{ex}}/\kappa_{\text{tot}} \sim 0.85$ at high gate voltages.

Application of negative gate voltage results in dramatic changes in resonator frequency [Fig. 1(b)], indicating that the JoFET contributes a gate-tunable inductance to the resonator. The resonant frequency can be tuned over more than 2 GHz of bandwidth [Fig. 1(c)], exhibiting weak voltage dependence at extremal values, characteristic of a transistor reaching pinch-off at negative voltage and saturation at positive voltage.

The internal dissipation rate κ_i and external coupling rates κ_{ex} also evolve with gate voltage. Near JoFET pinch off κ_i increases sharply, and κ_{ex} decreases over the same range [Fig. 2(a),2(b)]. The net effect is therefore a decrease in coupling efficiency near pinch-off, which limits the usable frequency range of the JoFET amplifier.

A plausible origin of the increase in κ_i is dissipation in the JoFET region. To test this hypothesis, we consider a minimal model of the JoFET as a parallel resistor R_J and inductor L_J [Fig. 2(b),inset], introducing an effective resistance $R_J/(\delta\phi)^2$ where $\delta\phi$ is the flux drop across the parallel combination. The flux drop can be inferred based on the measured resonant frequency, and couplings can then be calculated within an equivalent RLC model (see Appendix C).

Fitting κ_i to the circuit model results in satisfactory agreement with the data, with a best-fit shunt resistance $R_J = 14.0 \pm 0.2$ k Ω . Based on this agreement, we conclude that the junction presents dissipation to the circuit, with the practical effect of limiting performance at high inductances. We speculate that the dissipation is due to our use of a normal-conducting electrostatic gate, and is therefore not intrinsic to the Al-InAs system. The simple RLC model captures gate dependence of κ_{ex} at a qualitative level [Fig. 2(b)], although observed gate-dependence exceeds theoretical expectations. This discrepancy may reflect the role of extra capacitance in the JoFET region introduced by the electrostatic gate, which is not accounted for in the model.

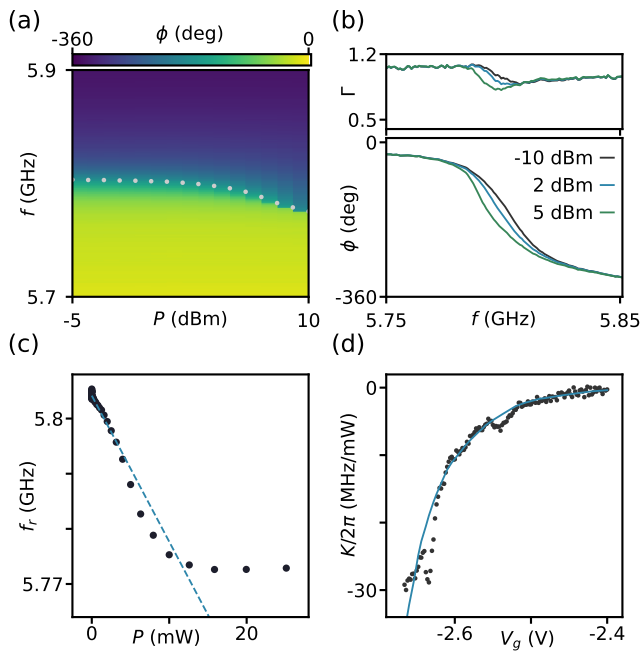


Figure 3. Nonlinear response. (a) Reflected signal phase ϕ versus signal power P and frequency f . White dots indicate resonant frequencies f_r . (b) Reflected magnitude Γ (top) and phase ϕ (bottom) versus f at different signal powers: low (black), medium (blue), and close to critical power (green). (c) Estimation of Kerr nonlinearity: resonant frequencies extracted from (a) versus average network analyzer power applied at room temperature (dots). Slope of linear fit (dashed line) gives an estimate of the Kerr coefficient. (d) Measured gate-dependent Kerr coefficient (black dots), and expected value from the parallel RL model, fit for a single power calibration factor. Kerr coefficient is expressed as a frequency shift per room-temperature VNA power. Different dataset from (c).

IV. NONLINEARITIES AND AMPLIFICATION

In addition to tunable inductance, the presence of the JoFET imparts a power-driven nonlinearity to the resonator [38]. Measuring the reflected phase as a function of signal frequency and power reveals that the resonant frequency smoothly decreases with increasing power [Fig. 3(a)]. The output power from microwave sources is related to the resonator input power by an estimated total attenuation of 110 dB for all measurements. The downward shift in resonant frequency is accompanied by “sharpening” of the phase response [Fig. 3(b)]. Downward shift in resonant frequency and an alteration in lineshape are key qualitative signatures of the required Kerr nonlinearity K for parametric amplification. The Kerr nonlinearity is estimated by measuring the change in resonant frequency per incident power in the low power limit, as shown by the linear fit in Fig. 3(c). Following this procedure at different gate voltages reveal that the nonlinearity is tunable with voltage, increasing in magnitude as gate voltage is decreased Fig. 3(d), mirroring

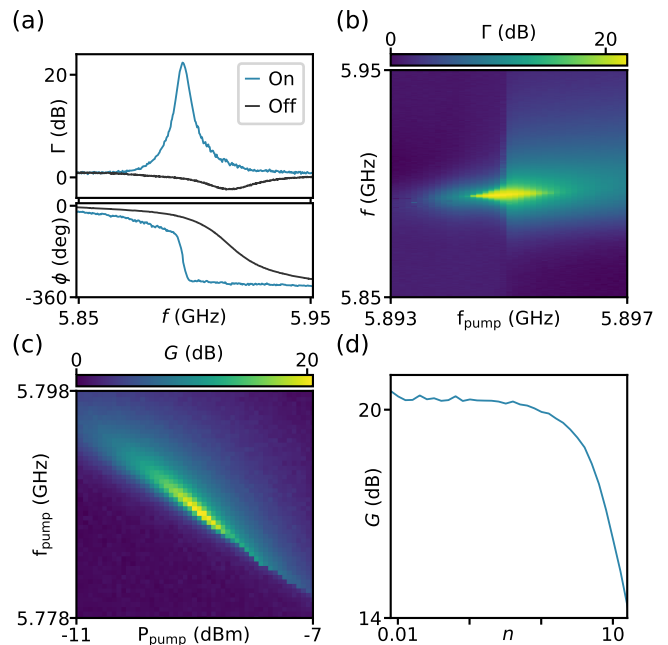


Figure 4. Parametric gain. (a) Reflected signal magnitude Γ and phase ϕ measured as a function of signal frequency f from bare resonator (black) and pumped resonator (blue). (b) Γ measured as a function of pump frequency f_{pump} and signal frequency f . The pump power is fixed slightly below the critical pump power at which the system bifurcates. $V_g = -2.5$ V for (a)-(b). (c) Gain G inferred from the maximal reflected amplitude measured as a function of pump power P_{pump} and pump frequency f_{pump} , revealing line of maximum gain. $V_g = -2.55$ V. (d) Gain G measured as a function of estimated average intracavity photon number n . $n = 0.01$ is approximately equivalent to a VNA input power $P = -43$ dBm and input power of -153 dBm. $V_g = -2.35$ V, $f_{pump} = 5.942$ GHz, signal-pump-detuning $\delta f = 1$ MHz and remains within the 3.6 MHz instantaneous amplification bandwidth.

the decrease in circuit resonant frequency observed in Fig. 1c. Calculating the expected Kerr nonlinearity based on the frequency shift in Fig. 1(c) adequately accounts for the observed the gate-voltage dependence. The resulting calibration factor of 1.5×10^5 photons per Watt of vector network analyzer (VNA) power is, however, not consistent with our independently measured attenuation or power calibration. We speculate that this discrepancy is dominated by the propagation of systematic errors in our circuit-parameter estimate, which can cause large effects because the Kerr nonlinearity is a fourth-order effect.

Parametric amplification is generated by applying a strong pump tone red detuned from the bare resonant frequency, in the vicinity of the phase “sharpening” features already identified close to the critical power Fig. 3(b). Measuring scattering parameters with a weak probe signal reveals in excess of 20 dB of gain with a 4 MHz bandwidth, and a sharp phase response typical of a parametric amplifier [Fig. 4(a),4(b)]. Modest detunings in the

pump frequency do not substantially affect the amplifier response, but for large deviations the gain decreases to unity [Fig. 4(b)]. Measuring the amplifier gain G as a function of pump frequency f_{pump} and power P_{pump} reveals a continuous region of maximum gain with an easily identifiable optimum operating region, as expected for a parametric amplifier [Fig. 4(c)]. The gate voltages used for the gain optimization and measurement shown in Fig. 4(a),4(b) and in Fig. 4(c),4(d) are different due to gate instability and hysteresis. After setting the gate voltages, it typically takes 15 minutes for the resonance to stabilize. Consequently, the resonant frequency remains stable for circa an hour which is just sufficient for our gain and noise measurements. When the resonant frequency drifts away, retrieval of amplification requires tuning up the pump frequency and amplitude again. We anticipate that optimization of the gate dielectric can greatly improve stability in future devices. The power handling capability of the amplifier is quantified by measuring the gain for different signal powers [Fig. 4(d)]. At very low input signal power where the average intracavity photon number is 0.01 [Fig. 4(d)], the gain saturates at 20.3 dB. Large input powers cause the amplifier gain to decrease, giving a 1 dB compression point of 2.9 intracavity photons [input power of -125 dBm, Fig. 4(d)]. The gain, bandwidth, and compression point are comparable to values obtained with early, practically useful parametric amplifiers based on metallic Al/AlOx Josephson junctions [7, 8, 39].

Quantum signals typically consist of few photons, making it crucial to achieve noise performance near the quantum limit. To assess the noise performance of the JoFET amplifier, a weak pilot signal is measured first with a commercial HEMT amplifier, and then with parametric gain activated [Fig. 5(a)]. The JoFET amplifier dramatically improves the signal-to-noise ratio (SNR) of the pilot-signal measurement. The total input-referred noise of the JoFET amplifier and subsequent measurement chain approaches the limits placed by quantum mechanics of a photon from nondegenerate amplification [2, 3]. At small detunings we find a noise temperature of 0.38 ± 0.2 K, which is consistent with the expected total value 0.40 ± 0.1 K from vacuum fluctuations (0.29 K), nonzero cavity loss at this gate voltage (0.09 ± 0.01 K), and input-referred noise from the classical measurement chain (0.02 K).

This noise measurement was carefully calibrated by varying the temperature of the mixing-chamber stage of the dilution refrigerator and measuring noise at various frequencies with the JoFET amplifier off [Fig. 5(b)]. In the high temperature limit, the output noise is linear in temperature, with an offset that reflects the added noise of the chain referred to the mixing chamber plate, giving $T_{H,MC} = 1.61$ K at the JoFET operating frequency. At low temperature input-referred noise saturates. Calibrating over a wide range of frequencies reveals that noise saturation is pronounced only for high frequencies, confirming that the saturation is due to quantum, as op-

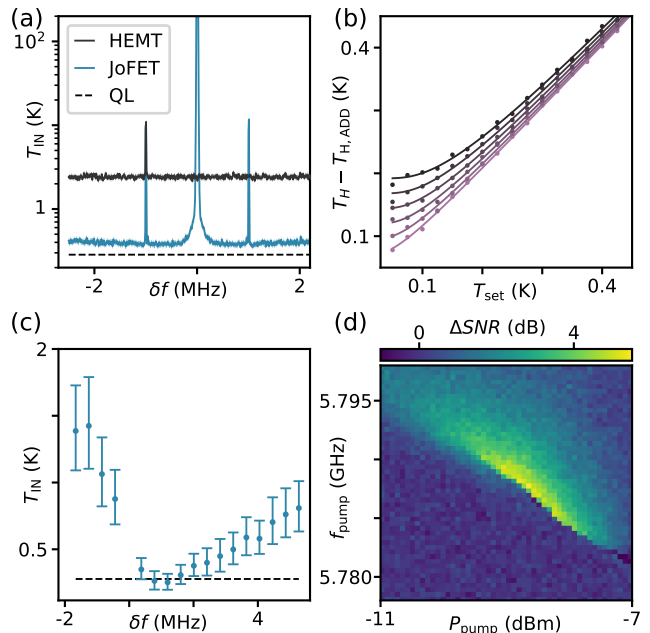


Figure 5. Quantum-limited operation. (a) Total noise temperature referred to JoFET input T_{IN} , measured in the presence of a weak pilot tone, as a function of detuning frequency from pump δf . Pump off (HEMT, black) and pump on (JoFET, blue) shown, in comparison with the quantum limit from input vacuum fluctuations and phase-preserving amplification (QL, dashed). $V_g = -2.35$ V. In JoFET data, the blue-detuned idler and the zero-detuned pump are also visible. Bands represent propagated uncertainty from cavity parameters, insertion loss measurements, and HEMT noise calibration. Note that here HEMT data are referred to cavity input, not HEMT input. (b) Added noise of chain without JoFET, referred to HEMT input. Difference between total noise temperature T_H and HEMT added noise $T_{H,ADD}$ measured as a function of mixing chamber temperature setpoint T_{set} . Lines represent unity slope due to Johnson-Nyquist noise, corrected for the presence of vacuum fluctuations which dominate at low temperature and high frequency [3]. (c) T_{IN} measured as a function of pump-signal detuning δf by varying pump frequency with signal frequency fixed. One datapoint with a detuning of 2.7 kHz had to be removed from the dataset since the pump and signal could not be resolved individually. Error bars represent uncertainty propagated through from circuit parameters and HEMT noise calibration. (d) Relative improvement in signal to noise ratio (ΔSNR) measured as a function of pump frequency f_{pump} and pump power P_{pump} : signal-pump detuning is fixed at 0.5 MHz, signal power is fixed at -43 dBm equivalent to 0.01 intracavity photon. $V_g = -2.55$ V for (c)-(d).

posed to thermal, fluctuations [3], and that these fluctuations are faithfully resolved by our calibration procedure. To find the noise referred to the JoFET input, T_{IN} , we divide by the independently measured insertion loss of all components in-between the JoFET input and the mixing chamber plate, including resonator loss (see Appendix H). This calibration procedure counts resonator

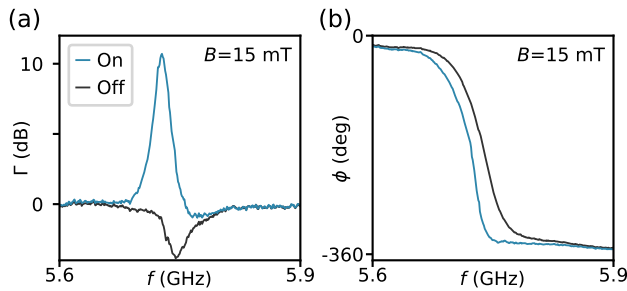


Figure 6. Magnetic field compatibility. Reflected magnitude Γ and (a), and phase ϕ (b) with and without pump tone as a function of probe frequency f in the presence of an in-plane magnetic field, $B = 15$ mT.

and sample-holder insertion loss against the performance of the JoFET amplifier, resulting in a noise temperature that represents the JoFET added noise referred to its input, which is a suitable quantity for characterizing the JoFET as a standalone device. It is not a measurement of total system efficiency, which would also need to include cable and circulator losses between a specified 50Ω load and the JoFET.

Changing the pump frequency while keeping the signal frequency fixed at 5.7839 GHz reveals that the noise performance is degraded if the pump frequency is away from the optimal operation region [Fig. 5(c)]. Note that this dataset was taken at a gate voltage with less resonator loss, yielding data that reach the quantum limit to within experimental uncertainty, albeit with a larger propagated uncertainty than in Fig. 5(a). By sweeping the pump frequency and the pump power with a fixed signal detuning, the optimum operating points of the amplifier can be extracted [Fig. 5(d)]. The operating points with best noise performance corresponds to the regions of highest gain identified in Fig. 4(c), as expected.

V. MAGNETIC FIELD OPERATION

A technical advantage conferred by the Al-InAs hybrid platform is compatibility with external magnetic fields. To explore the magnetic-field compatibility of the JoFET amplifier, we have steadily increased the parallel external magnetic field to 15 mT while compensating for small field misalignments with a perpendicular magnetic coil. Even with compensation, the resonator parameters evolve slightly in magnetic field, and a slight increase in loss is observed. Applying a pump tone gives an optimized gain of 10 dB [Fig. 6(a)-6(b)]. This demonstrates parametric amplification at a magnetic field order of magnitudes larger than the typical operating value for tunable metallic superconducting parametric amplifiers. Future experiments need to improve the resonator stability in magnetic field in order to allow a reliable noise measurement; we were unable to demonstrate quantum-limited operation in a magnetic field. The most likely rea-

son for this is the depinning of trapped flux by high pump powers. This effect can be removed by forming the resonator center pin from a field-compatible superconductor that connects to a smaller Al-InAs microstructure, as was done with recent field-compatible superconducting qubits [40].

VI. OUTLOOK

Summarizing, we have demonstrated a quantum-limited and JoFET amplifier, already obtaining performance comparable to traditional Al/AIOx devices in our initial, unoptimized device. A number of techniques are available to further improve the performance of our device. The participation factor of the superconductor-semiconductor heterostructure can be reduced drastically by working with a small mesa in the JoFET region. This would likely decrease microwave losses, and allow the use of field-resilient superconductors like NbTi, which should allow operations in external magnetic fields of order 1 Tesla. The number of JoFETs and the designed critical current can also be adapted to provide the target nonlinearity at milder gate voltages [38]. Device dissipation can also likely be improved by using a superconducting electrostatic gate with on-chip filters. Finally, superconducting-semiconducting hybrid material systems are being actively developed so material-level improvements can be expected.

Our work opens up the new, general direction of quantum-limited signal processing devices based on semiconductors, and can be expanded to devices such as [39, 41] circulators [42, 43] or signal generators [44]. An appealing advantage of a semiconductor platform is the possibility of tight integration with semiconductor-based quantum devices, for instance spin qubits, or CMOS-based quantum control solutions [25–27]. It is also interesting to note that the electrostatic gate can be viewed as a receiver for high-impedance electrical signals, suggesting applications such as electrometry with an integrated, quantum-limited amplifier.

During preparation of this manuscript we became aware of related works demonstrating parametric amplification with graphene weak links [45, 46].

Acknowledgements We thank Shyam Shankar for helpful feedback on the manuscript. We gratefully acknowledge the support of the ISTA nanofabrication facility, MIBA machine shop and e-machine shop. NYU team acknowledges support from Army Research Office grant no. W911NF2110303.

Data availability Raw data for all plots in the main text and supplement will be included with the manuscript before publication. Further data available upon reasonable request.

Appendix A: Sample preparation

The JoFET amplifier was fabricated from Al-proximitized InAs quantum well which was grown on a semi-insulating, Fe counter-doped (100) InP wafer. All the patterns were transferred with Raith EBPG 5100 electron beam lithography system. The Josephson weak link was made by etching a trench in the aluminum layer in the commercial etchant Transene D at 50 degrees C for 5 seconds. The trench was designed to be 20 nm long and 25 μm wide. SEM imaging later showed that the trench width was about 50 nm. The superconductor-semiconductor mesa forming the center pin of the CPW resonator was formed by masking with PMMA followed by a semiconductor wet etch in a mixture of $\text{CH}_3\text{COOH} : \text{H}_2\text{O}_2 : \text{H}_3\text{PO}_4$ for 150 seconds at room temperature. The ground plane was constructed by evaporating Ti 5 nm, Nb 50 nm following a short 1-min Ar ion milling at an accelerating voltage of 400 V, with an ion current of 21 mA in a Plassys UHV evaporator. In the next step, the dielectric layer separating the gate and the junction was deposited with an Oxford ALD system running a thermal ALD alumina process at 150 degrees C in 150 cycles, which gave an approximated thickness of 12 nm. Eventually, the gate that covers just the area of the Josephson weak link was created by evaporating Ti 8 nm and Au 80 nm at a tilt angle of 30 degrees with 5 RPM planetary rotation in a Plassys HV evaporator. Due to low adhesion of Al bond wire to Nb ground plane, co-deposited Au bond pads are used to enhance Al alloy formation during wire bonding, hence, chip-to-chip bond yield. All lift-off and cleaning processes were performed in hot acetone at 50 degrees C and isopropanol.

Appendix B: Measurements

The sample was mounted on a copper bracket on a home made printed circuit board. We used a vector network analyzer (VNA) model Keysight P9372A to measure R . A Rohde & Schwarz signal generator model SGS100A was used to provide the pump tone. When pumping at a fixed frequency, we used the VNA to provide a small probe signal and measure the gain profile from the reflected monotone at probe frequency. A home-made IVVI voltage source provided the gate bias. To achieve gain, we typically set the gate voltage to -2.5 V and swept the VNA power until the response became critical. Consequentially, a pump tone from the R&S signal generator was injected at a power of about 1 dB below the approximated critical power and slightly above the critical frequency. The probe power from the VNA was reduced to maintain the validity of the stiff pump condition. We tuned up the JoFET amplifier by sweeping the pump frequency and power in the proximity of the nonlinear resonator's critical values and recording the maximal reflected amplitude at the VNA input. Optimal amplification configurations were then found by fine sweeping

around the regions where the maximal gains were highest, whose values were typically more than 20 dB. To measure the noise, we recorded the power spectral density from the output of the JoFET amplifier by a ThinkRF R5550 hybrid spectrum analyzer. In-plane magnetic field and compensation was applied by a vector magnet system of the Oxford Triton fridge and Mercury iPS power supply.

Appendix C: RLC circuit model

To model gate-dependence of κ_{ex} and κ_i in Fig. 2 we find an effective lumped-element representation of the circuit, and then couple it to transmission lines following the procedure in Ref. [47].

Our circuit can be imagined as two resonators of length l and inductance per unit length L_l , capacitance per unit length C_l , and attenuation constant α coupled through the parallel RL circuit. For a large shunt resistance the inductance of the parallel combination is given by L_J . The model therefore introduces dissipation without changing the resonant frequency. The resonant wave vector k satisfies [48]

$$2 \cot(kl) = -\frac{L_J}{L_l} kl. \quad (\text{C1})$$

The effective capacitance is [38]

$$C_{\text{eff}} = C_l l (1 + \text{sinc}(2kl)). \quad (\text{C2})$$

We do not know of an explicit treatment of dissipation in our geometry available in the literature, so in analogy with the definition of C_{eff} we model it with the effective resistance is $R_J/(\delta\phi)^2$, where $\delta\phi = 2 \cos(kl)$ is the flux drop across the resistor. The internal dissipation and external coupling rates are then

$$\kappa_i = \frac{\alpha l}{Z_0 C_{\text{eff}}} + \frac{(\delta\phi)^2}{R_J C_{\text{eff}}} \quad (\text{C3})$$

$$\kappa_{\text{ex}} = \frac{1}{R^* C_{\text{eff}}}, \quad (\text{C4})$$

where $R^* = (1 + \omega_k^2 C_k^2 Z_0^2)/(\omega_k^2 C_k^2 Z_0)$ is the effective parallel resistance from the measurement port with impedance Z_0 coupled with capacitance C_k .

To fit this model we use the fact that $kl = (\pi/2)f/f_0$ where f_0 is the resonant frequency of the CPW resonator when L_J is zero. We estimate $f_0 = 6$ GHz and then extract kl directly from the measured data. We fix the characteristic impedance of the resonator as $Z_0 = 60 \Omega$ based on the difference between the designed and observed resonant frequency, which we attribute to the kinetic inductance of the heterostructure [37]. Knowledge of kl , f_0 , and Z_0 allows the effective capacitance and Josephson inductance to be calculated. Eq. C3 is fit for α and R_J in Fig. 2(a) and Eq. C4 is fit for C_k .

Appendix D: Conversion from signal power to average intracavity photon number

The average intra-cavity photon number n is linearly dependent on the incident power P_{in} at the input port:

$$n = \frac{1}{\hbar f_s} \frac{4\kappa_{ex} P_{in}}{(\kappa_{ex} + \kappa_i)^2 + 4\Delta^2}. \quad (\text{D1})$$

The input power is estimated based on the VNA power and the total attenuation A of the setup.

Appendix E: Total attenuation estimate

The total attenuation A between the output of the VNA and the input of the device is calculated from noise spectrum from the measurement port with a signal tone at -43 dBm output power. The noise floor is identified with input-referred noise temperature $T_{H,MC} = 1.61$ K from the HEMT calibration measurement shown in Fig. 5(b), combined with the resolution bandwidth of the signal analyzer $BW = 3.88$ kHz, giving $P_{noise} = 10 \log(k_B T_N BW / (1 \text{ mW})) = -160.6$ dBm. The signal is 6.3 dB above the noise floor, so its input referred magnitude is -153 dBm. Accounting for the small -0.84 dB of loss from the (detuned) cavity then gives the total attenuation $A = -110$ dB quoted in the main text.

Appendix F: Kerr nonlinearity extraction from power sweep

The dependence of resonance frequency on input power was used to estimate the Kerr nonlinearity K similar to [7]. Resonant frequency decreased linearly with increasing average intracavity photon number following the Hamiltonian [38]:

$$H_{JPA} = \hbar \left(\tilde{\omega}_0 + \frac{K}{2} \langle A^\dagger A \rangle \right) A^\dagger A. \quad (\text{F1})$$

The slope of the line in Fig. 3(c) measures $K/2$.

Appendix G: JoFET amplifier design

CPW resonator was designed to have a characteristic impedance of 50Ω with the center conductor with and gap of $25 \mu\text{m}$ and $16 \mu\text{m}$. Resonator length was chosen so that the target resonant frequency of 6 GHz would be achieved at base temperature. To account for the kinetic inductance of the 10 nm-thick Al layer, geometric resonant frequency was designed to be 7.2 GHz so that result resonance would drop to 6 GHz based on previous fabrication experience. The kinetic inductance of the Al film fluctuates from device to device, presumably due to uncontrolled oxidation of the Al. The JoFET was designed for a maximal critical current of $10 \mu\text{A}$ which gives

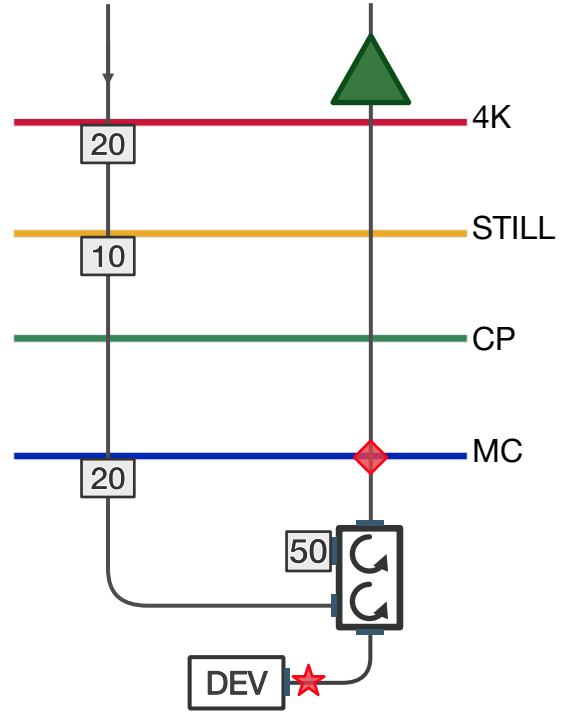


Figure 7. Schematic of insertion loss calibration. Noise referred to point \diamond is referred to device input \star by measuring the cold insertion loss of each component.

a zeroth order Kerr nonlinearity K of 1.4 kHz at zero bias and in this CPW configuration, such that the device can be gated into a regime appropriate for amplification [38]. Designed dimensions were chosen based on our previous lithography tests and critical current measurements where a sheet critical current density of $0.38 \mu\text{A}/\mu\text{m}$ was achieved.

Appendix H: JoFET input noise referral

The temperature sweep in Fig. 5(b) is used to refer HEMT noise to the mixing chamber plate [point \diamond in Fig. 7]. Noise is then referred to device input [point \star in Fig. 7] by measuring the insertion loss η of the components in the signal path: the circulators, coaxial cables, sample board, and device. When the JoFET amplifier is off, noise at \diamond is related to noise at \star according to $S_\diamond = \eta S_\star + (1 - \eta)V + T_{H,MC}$, where the second term represents the introduction of vacuum noise V by loss. The input-referred noise is then S_\diamond/η , which in the special case of vacuum-noise input gives $(T_{H,MC} + V)/\eta$.

We measured the transmission of the cable-circulator combination to be 0.6 dB and the sample holder insertion reflected insertion loss to be 0.2 dB. With the JoFET amplifier off, there is 0.6 dB of insertion loss from the detuned circuit resonance. This results in a total insertion loss of $\eta = 0.72$ between \star and \diamond . Referring the added noise of the HEMT and vacuum fluctuations V

back to device input gives the black line in Fig. 5(a), with a typical value of $(T_{H,MC} + V)/\eta \sim 2.42$ K.

When the JoFET amplifier is on, the additional gain must be divided out, which is measured using the pilot tone in Fig. 5(a). We determine the JoFET amplifier

frequency response from a Lorentzian fit to the measured noise spectrum, and determine the overall gain level from the pilot signals, accounting for their nonzero detuning. Noise is input-referred by dividing by the full JoFET gain profile and the cable-circulator insertion loss.

-
- [1] H. A. Haus and J. A. Mullen, “Quantum noise in linear amplifiers,” *Phys. Rev.* **128**, 2407–2413 (1962).
- [2] Carlton M. Caves, “Quantum limits on noise in linear amplifiers,” *Phys. Rev. D* **26**, 1817–1839 (1982).
- [3] A. A. Clerk, M. H. Devoret, S. M. Girvin, Florian Marquardt, and R. J. Schoelkopf, “Introduction to quantum noise, measurement, and amplification,” *Rev. Mod. Phys.* **82**, 1155–1208 (2010).
- [4] B. Yurke, L. R. Corruccini, P. G. Kaminsky, L. W. Rupp, A. D. Smith, A. H. Silver, R. W. Simon, and E. A. Whittaker, “Observation of parametric amplification and deamplification in a josephson parametric amplifier,” *Phys. Rev. A* **39**, 2519–2533 (1989).
- [5] R. Movshovich, B. Yurke, P. G. Kaminsky, A. D. Smith, A. H. Silver, R. W. Simon, and M. V. Schneider, “Observation of zero-point noise squeezing via a josephson-parametric amplifier,” *Phys. Rev. Lett.* **65**, 1419–1422 (1990).
- [6] B. Yurke, M. L. Roukes, R. Movshovich, and A. N. Pargellis, “A low-noise series-array josephson junction parametric amplifier,” *Applied Physics Letters* **69**, 3078–3080 (1996), <https://doi.org/10.1063/1.116845>.
- [7] M. A. Castellanos-Beltran and K. W. Lehnert, “Widely tunable parametric amplifier based on a superconducting quantum interference device array resonator,” *Applied Physics Letters* **91**, 083509 (2007), <https://doi.org/10.1063/1.2773988>.
- [8] M. A. Castellanos-Beltran, K. D. Irwin, G. C. Hilton, L. R. Vale, and K. W. Lehnert, “Amplification and squeezing of quantum noise with a tunable josephson metamaterial,” *Nature Physics* **4**, 929–931 (2008).
- [9] N. Bergeal, F. Schackert, M. Metcalfe, R. Vijay, V. E. Manucharyan, L. Frunzio, D. E. Prober, R. J. Schoelkopf, S. M. Girvin, and M. H. Devoret, “Phase-preserving amplification near the quantum limit with a josephson ring modulator,” *Nature* **465**, 64–68 (2010).
- [10] C. Macklin, K. O’Brien, D. Hover, M. E. Schwartz, V. Bolkhovskiy, X. Zhang, W. D. Oliver, and I. Siddiqi, “A near-quantum-limited josephson traveling-wave parametric amplifier,” *Science* **350**, 307–310 (2015), <https://www.science.org/doi/pdf/10.1126/science.aaa8525>.
- [11] Luca Planat, Arpit Ranadive, Rémy Dassonneville, Javier Puertas Martínez, Sébastien Léger, Cécile Naud, Olivier Buisson, Wiebke Hasch-Guichard, Denis M. Basko, and Nicolas Roch, “Photonic-crystal josephson traveling-wave parametric amplifier,” *Phys. Rev. X* **10**, 021021 (2020).
- [12] N. E. Frattini, V. V. Sivak, A. Lingenfelter, S. Shankar, and M. H. Devoret, “Optimizing the nonlinearity and dissipation of a snail parametric amplifier for dynamic range,” *Phys. Rev. Applied* **10**, 054020 (2018).
- [13] J. Shabani, M. Kjaergaard, H. J. Suominen, Younghyun Kim, F. Nichele, K. Pakrouski, T. Stankevic, R. M. Lutchyn, P. Krogstrup, R. Feidenhans’l, S. Kraemer, C. Nayak, M. Troyer, C. M. Marcus, and C. J. Palmstrøm, “Two-dimensional epitaxial superconductor-semiconductor heterostructures: A platform for topological superconducting networks,” *Phys. Rev. B* **93**, 155402 (2016).
- [14] Wendy L. Sarney, Stefan P. Svensson, Kaushini S. Wickramasinghe, Joseph Yuan, and Javad Shabani, “Reactivity studies and structural properties of al on compound semiconductor surfaces,” *Journal of Vacuum Science & Technology B* **36**, 062903 (2018), <https://doi.org/10.1116/1.5053987>.
- [15] Wendy L. Sarney, Stefan P. Svensson, Asher C. Leff, William F. Schiela, Joseph O. Yuan, Matthieu C. Dartailh, William Mayer, Kaushini S. Wickramasinghe, and Javad Shabani, “Aluminum metallization of iii–v semiconductors for the study of proximity superconductivity,” *Journal of Vacuum Science & Technology B* **38**, 032212 (2020), <https://doi.org/10.1116/1.5145073>.
- [16] M. Kjaergaard, F. Nichele, H. J. Suominen, M. P. Nowak, M. Wimmer, A. R. Akhmerov, J. A. Folk, K. Flensberg, J. Shabani, C. J. Palmstrøm, and C. M. Marcus, “Quantized conductance doubling and hard gap in a two-dimensional semiconductor–superconductor heterostructure,” *Nature Communications* **7**, 12841 (2016).
- [17] William Mayer, Joseph Yuan, Kaushini S. Wickramasinghe, Tri Nguyen, Matthieu C. Dartailh, and Javad Shabani, “Superconducting proximity effect in epitaxial al–inas heterostructures,” *Applied Physics Letters* **114**, 103104 (2019).
- [18] Matthieu C. Dartailh, Joseph J. Cuzzo, Bassel H. Elfeky, William Mayer, Joseph Yuan, Kaushini S. Wickramasinghe, Enrico Rossi, and Javad Shabani, “Missing shapiro steps in topologically trivial josephson junction on InAs quantum well,” *Nature Communications* **12**, 78 (2021).
- [19] Fabrizio Nichele, Asbjørn C. C. Drachmann, Alexander M. Whiticar, Eoin C. T. O’Farrell, Henri J. Suominen, Antonio Fornieri, Tian Wang, Geoffrey C. Gardner, Candice Thomas, Anthony T. Hatke, Peter Krogstrup, Michael J. Manfra, Karsten Flensberg, and Charles M. Marcus, “Scaling of majorana zero-bias conductance peaks,” *Phys. Rev. Lett.* **119**, 136803 (2017).
- [20] Antonio Fornieri, Alexander M. Whiticar, F. Setiawan, Elías Portolés, Asbjørn C. C. Drachmann, Anna Keselman, Sergei Gronin, Candice Thomas, Tian Wang, Ray Kallaher, Geoffrey C. Gardner, Erez Berg, Michael J. Manfra, Ady Stern, Charles M. Marcus, and Fabrizio Nichele, “Evidence of topological superconductivity in planar josephson junctions,” *Nature* **569**, 89–92 (2019).
- [21] Matthieu C. Dartailh, William Mayer, Joseph Yuan, Kaushini S. Wickramasinghe, Alex Matos-Abiague, Igor Žutić, and Javad Shabani, “Phase signature of topological transition in josephson junctions,” *Phys. Rev. Lett.* **126**, 036802 (2021).

- [22] Morteza Aghaee, Arun Akkala, Zulfi Alam, Rizwan Ali, Alejandro Alcaraz Ramirez, Mariusz Andrzejczuk, Andrey E Antipov, Pavel Aseev, Mikhail Astafev, Bela Bauer, Jonathan Becker, Srini Boddapati, Frenk Boekhout, Jouri Bommer, Esben Bork Hansen, Tom Bosma, Leo Bourdet, Samuel Boutin, Philippe Caroff, Lucas Casparis, Maja Cassidy, Anna Wulf Christensen, Noah Clay, William S Cole, Fabiano Corsetti, Ajuan Cui, Paschalis Dalampiras, Anand Dokania, Gijs de Lange, Michiel de Moor, Juan Carlos Estrada Saldaña, Saeed Fallahi, Zahra Heidarnia Fathabad, John Gamble, Geoff Gardner, Deshan Govender, Flavio Griggio, Ruben Grigoryan, Sergei Gronin, Jan Gukelberger, Sebastian Heedt, Jesús Herranz Zamorano, Samantha Ho, Ulrik Laurens Holgaard, William Hvidtfelt Padkær Nielsen, Henrik Ingerslev, Peter Jeppesen Krogstrup, Linda Johansson, Jeffrey Jones, Ray Kallaher, Farhad Karimi, Torsten Karzig, Cameron King, Maren Elisabeth Kloster, Christina Knapp, Dariusz Kocon, Jonne Koski, Pasi Kostamo, Mahesh Kumar, Tom Laeven, Thorvald Larsen, Kongyi Li, Tyler Lindemann, Julie Love, Roman Lutchny, Michael Manfra, Elvedin Memisevic, Chetan Nayak, Bas Nijholt, Morten Hannibal Madsen, Signe Markussen, Esteban Martinez, Robert McNeil, Andrew Mullally, Jens Nielsen, Anne Nurmohamed, Eoin O'Farrell, Keita Otani, Sebastian Pauka, Karl Petersson, Luca Petit, Dima Pikulin, Frank Preiss, Marina Quintero Perez, Katrine Rasmussen, Mohana Rajpalke, Davydas Razmadze, Outi Reentila, David Reilly, Richard Rouse, Ivan Sadovskyy, Lauri Sainiemi, Sydney Schreppler, Vadim Sidorkin, Amrita Singh, Shilpi Singh, Sarat Sinha, Patrick Sohr, Tomaš Stankevič, Lieuwe Stek, Henri Suominen, Judith Suter, Vicky Svidenko, Sam Teicher, Mine Temuerhan, Nivetha Thiyagarajah, Raj Tholapi, Mason Thomas, Emily Toomey, Shivendra Upadhyay, Ivan Urban, Saulius Vaitiekėnas, Kevin Van Hoogdalem, Dmitrii V. Viazmitinov, Steven Waddy, David Van Woerkom, Dominik Vogel, John Watson, Joseph Weston, Georg W. Winkler, Chung Kai Yang, Sean Yau, Daniel Yi, Emrah Yucelen, Alex Webster, Roland Zeisel, and Ruichen Zhao, "Inas-al hybrid devices passing the topological gap protocol," [arXiv:2207.02472](https://arxiv.org/abs/2207.02472) (2022).
- [23] C. G. L. Böttcher, F. Nichele, M. Kjaergaard, H. J. Suominen, J. Shabani, C. J. Palmstrøm, and C. M. Marcus, "Superconducting, insulating and anomalous metallic regimes in a gated two-dimensional semiconductor-superconductor array," *Nature Physics* **14**, 1138–1144 (2018).
- [24] Lucas Casparis, Malcolm R. Connolly, Morten Kjaergaard, Natalie J. Pearson, Anders Kringhøj, Thorvald W. Larsen, Ferdinand Kuemmeth, Tiantian Wang, Candice Thomas, Sergei Gronin, Geoffrey C. Gardner, Michael J. Manfra, Charles M. Marcus, and Karl D. Petersson, "Superconducting gatemon qubit based on a proximitized two-dimensional electron gas," *Nature Nanotechnology* **13**, 915–919 (2018).
- [25] Simon Schaal, Alessandro Rossi, Virginia N. Ciriano-Tejel, Tsung-Yeh Yang, Sylvain Barraud, John J. L. Morton, and M. Fernando Gonzalez-Zalba, "A cmos dynamic random access architecture for radio-frequency readout of quantum devices," *Nature Electronics* **2**, 236–242 (2019).
- [26] S. J. Pauka, K. Das, R. Kalra, A. Moini, Y. Yang, M. Trainer, A. Bousquet, C. Cantaloube, N. Dick, G. C. Gardner, M. J. Manfra, and D. J. Reilly, "A cryogenic cmos chip for generating control signals for multiple qubits," *Nature Electronics* **4**, 64–70 (2021).
- [27] Xiao Xue, Bishnu Patra, Jeroen P. G. van Dijk, Nodar Samkharadze, Sushil Subramanian, Andrea Corna, Brian Paquelet Wuetz, Charles Jeon, Farhana Sheikh, Esdras Juarez-Hernandez, Brando Perez Esparza, Huzaifa Rampurawala, Brent Carlton, Surej Ravikummar, Carlos Nieva, Sungwon Kim, Hyung-Jin Lee, Amir Sammak, Giordano Scappucci, Menno Veldhorst, Fabio Sebastiani, Masoud Babaie, Stefano Pellerano, Edoardo Charbon, and Lieven M. K. Vandersypen, "Cmos-based cryogenic control of silicon quantum circuits," *Nature* **593**, 205–210 (2021).
- [28] F. Lecocq, F. Quinlan, K. Cicak, J. Aumentado, S. A. Diddams, and J. D. Teufel, "Control and readout of a superconducting qubit using a photonic link," *Nature* **591**, 575–579 (2021).
- [29] T. W. Larsen, K. D. Petersson, F. Kuemmeth, T. S. Jespersen, P. Krogstrup, J. Nygård, and C. M. Marcus, "Semiconductor-nanowire-based superconducting qubit," *Phys. Rev. Lett.* **115**, 127001 (2015).
- [30] M. Veldhorst, J. C. C. Hwang, C. H. Yang, A. W. Leenstra, B. de Ronde, J. P. Dehollain, J. T. Muhonen, F. E. Hudson, K. M. Itoh, A. Morello, and A. S. Dzurak, "An addressable quantum dot qubit with fault-tolerant control-fidelity," *Nature Nanotechnology* **9**, 981–985 (2014).
- [31] Kenta Takeda, Jun Kamioka, Tomohiro Otsuka, Jun Yoneda, Takashi Nakajima, Matthieu R. Delbecq, Shinichi Amaha, Giles Allison, Tetsuo Koder, Shunri Oda, and Seigo Tarucha, "A fault-tolerant addressable spin qubit in a natural silicon quantum dot," *Science Advances* **2**, e1600694 (2016), <https://www.science.org/doi/pdf/10.1126/sciadv.1600694>.
- [32] Jun Yoneda, Kenta Takeda, Tomohiro Otsuka, Takashi Nakajima, Matthieu R. Delbecq, Giles Allison, Takumu Honda, Tetsuo Koder, Shunri Oda, Yusuke Hoshi, Noritaka Usami, Kohei M. Itoh, and Seigo Tarucha, "A quantum-dot spin qubit with coherence limited by charge noise and fidelity higher than 99.9%," *Nature Nanotechnology* **13**, 102–106 (2018).
- [33] Akito Noiri, Kenta Takeda, Takashi Nakajima, Takashi Kobayashi, Amir Sammak, Giordano Scappucci, and Seigo Tarucha, "Fast universal quantum gate above the fault-tolerance threshold in silicon," *Nature* **601**, 338–342 (2022).
- [34] Xiao Xue, Maximilian Russ, Nodar Samkharadze, Brennan Undseth, Amir Sammak, Giordano Scappucci, and Lieven M. K. Vandersypen, "Computing with spin qubits at the surface code error threshold," [arXiv:2107.00628](https://arxiv.org/abs/2107.00628) (2022).
- [35] N. Samkharadze, A. Bruno, P. Scarlino, G. Zheng, D. P. DiVincenzo, L. DiCarlo, and L. M. K. Vandersypen, "High-kinetic-inductance superconducting nanowire resonators for circuit qed in a magnetic field," *Phys. Rev. Applied* **5**, 044004 (2016).
- [36] J.G. Kroll, F. Borsoi, K.L. van der Enden, W. Uilhoorn, D. de Jong, M. Quintero-Pérez, D.J. van Woerkom, A. Bruno, S.R. Plissard, D. Car, E.P.A.M. Bakkers, M.C. Cassidy, and L.P. Kouwenhoven, "Magnetic-field-resilient superconducting coplanar-waveguide resonators for hybrid circuit quantum electrodynamics experiments," *Phys. Rev. Applied* **11**, 064053 (2019).
- [37] D. Phan, J. Senior, A. Ghazaryan, M. Hatefipour, W. M.

- Strickland, J. Shabani, M. Serbyn, and A. P. Higginbotham, “Detecting induced $p \pm ip$ pairing at the al-inas interface with a quantum microwave circuit,” *Phys. Rev. Lett.* **128**, 107701 (2022).
- [38] Christopher Eichler and Andreas Wallraff, “Controlling the dynamic range of a josephson parametric amplifier,” *EPJ Quantum Technology* **1**, 2 (2014).
- [39] N. Bergeal, R. Vijay, V. E. Manucharyan, I. Siddiqi, R. J. Schoelkopf, S. M. Girvin, and M. H. Devoret, “Analog information processing at the quantum limit with a josephson ring modulator,” *Nature Physics* **6**, 296–302 (2010).
- [40] A. Kringhøj, T. W. Larsen, O. Erlandsson, W. Uilhoorn, J.G. Kroll, M. Hesselberg, R.P.G. McNeil, P. Krogstrup, L. Casparis, C.M. Marcus, and K.D. Petersson, “Magnetic-field-compatible superconducting transmon qubit,” *Phys. Rev. Applied* **15**, 054001 (2021).
- [41] Benjamin J. Chapman, Eric I. Rosenthal, Joseph Kerckhoff, Leila R. Vale, Gene C. Hilton, and K. W. Lehnert, “Single-sideband modulator for frequency domain multiplexing of superconducting qubit readout,” *Applied Physics Letters* **110**, 162601 (2017), <https://doi.org/10.1063/1.4981390>.
- [42] Benjamin J. Chapman, Eric I. Rosenthal, Joseph Kerckhoff, Bradley A. Moores, Leila R. Vale, J. A. B. Mates, Gene C. Hilton, Kevin Lalumière, Alexandre Blais, and K. W. Lehnert, “Widely tunable on-chip microwave circulator for superconducting quantum circuits,” *Phys. Rev. X* **7**, 041043 (2017).
- [43] Benjamin J. Chapman, Eric I. Rosenthal, and K. W. Lehnert, “Design of an on-chip superconducting microwave circulator with octave bandwidth,” *Phys. Rev. Applied* **11**, 044048 (2019).
- [44] M. C. Cassidy, A. Bruno, S. Rubbert, M. Irfan, J. Kammhuber, R. N. Schouten, A. R. Akhmerov, and L. P. Kouwenhoven, “Demonstration of an ac josephson junction laser,” *Science* **355**, 939–942 (2017), <https://www.science.org/doi/pdf/10.1126/science.aah6640>.
- [45] Guilliam Butseraen, Arpit Ranadive, Nicolas Aparicio, Kazi Rafsanjani Amin, Abhishek Juyal, Martina Esposito, Kenji Watanabe, Takashi Taniguchi, Nicolas Roch, François Lefloch, and Julien Renard, “A gate-tunable graphene josephson parametric amplifier,” arXiv:2204.02175 (2022).
- [46] Joydip Sarkar, Kishor V. Salunkhe, Supriya Mandal, Subhamoy Ghatak, Alisha H. Marchawala, Ipsita Das, Kenji Watanabe, Takashi Taniguchi, R. Vijay, and Mandar M. Deshmukh, “Quantum noise limited microwave amplification using a graphene josephson junction,” arXiv:2204.02103 (2022), [10.48550/ARXIV.2204.02103](https://arxiv.org/abs/2204.02103).
- [47] M. Göppl, A. Fragner, M. Baur, R. Bianchetti, S. Filipp, J. M. Fink, P. J. Leek, G. Puebla, L. Steffen, and A. Wallraff, “Coplanar waveguide resonators for circuit quantum electrodynamics,” *Journal of Applied Physics* **104**, 113904 (2008), <https://doi.org/10.1063/1.3010859>.
- [48] J. Bourassa, F. Beaudoin, Jay M. Gambetta, and A. Blais, “Josephson-junction-embedded transmission-line resonators: From kerr medium to in-line transmon,” *Phys. Rev. A* **86**, 013814 (2012).